International Journal of Solids and Structures 340 (2026) 114220

Contents lists available at ScienceDirect

International Journal of Solids and Structures

journal homepage: www.elsevier.com/locate/ijsolstr

Control parameters for swelling-induced fracture in brittle polymer gels

Hongwei Wu [a], Alyssa VanZanten [b], Surbhi Punhani-Schillinger [b], Samira W. Khan [c], Michelle M. Driscoll [c], Caroline R. Szczepanski [b], Giuseppe Buscarnera [a,*]

[a] Department of Civil and Environmental Engineering, Northwestern University, Evanston, IL, USA
[b] Department of Chemical Engineering and Materials Science, Michigan State University, East Lansing, MI, USA
[c] Department of Physics and Astronomy, Northwestern University, Evanston, IL, USA

ARTICLE INFO

Keywords:
Brittle soft materials
Swelling-induced fracture
Chemoelasticity
Phase-field model
Dimensionless analysis

ABSTRACT

Soft materials such as brittle polymer gels can exhibit swelling-induced fracture when submerged in a solvent. Nevertheless, the factors that either hinder or promote fracture are not yet fully understood. This study aims to investigate this behavior through a chemoelastic phase-field model specifically designed to simulate simultaneous swelling and tensile failure. Uniaxial tension tests on single-edge-notched specimens of three crosslinking densities are then used to quantify the size sensitivity of brittle fracture in these materials, as well as their toughness. The calibrated model is shown to reproduce edge-initiated cracking arising from stress concentration and to capture crack propagation and stress-field evolution during swelling. Furthermore, a dimensionless analysis is conducted to identify four parameter groups. Two distinct regimes, diffuse swelling and self-rupture, are identified and validated by exploring the parameter space with the proposed numerical model. Considering the effect of the polymer composition on the mechanical properties, the results suggest that increasing crosslinking density yields counteracting effects that hinder self-rupture, whereas decreasing values of chain length do show potential for self-rupture. These insights shed light on the design and the possible tunability of brittle polymer gels with swelling-induced fracture behavior.

1. Introduction

Hydrophilic polymer gels such as hydrogels are distinguished by their ability to absorb and retain large quantities of solvent molecules, leading to significant volumetric expansion during swelling. Due to their broad application potential, researchers have developed numerous models to capture the swelling behavior of polymers, among which the Flory–Huggins and Flory-Rehner are the most widely recognized (Huggins, 1941; Flory, 1942; Flory and Rehner, 1943). Although these models capture the equilibrium state of swelling, they cannot resolve the transient swelling dynamics or the buildup of internal stresses which trigger instabilities and self-rupture during swelling (Leslie et al., 2021; VanZanten et al., 2024). To address these shortcomings, previous studies have embedded the Flory-type free energy in a poroelastic framework, coupling solvent diffusion with large-deformation solid mechanics (Hong et al., 2008; Chester and Anand, 2010; Bouklas and Huang, 2012). While nonlinear poroelasticity is preferred to describe large swelling and finite strains, the linear approximation remains valid when deformation is small (Bouklas and Huang, 2012; Yoon et al., 2010; Chen et al., 2020).

During the swelling process, polymer gels can not only exhibit surface instabilities such as wrinkles and creases (Ding et al., 2018; Bertrand et al., 2016; Dortdivanlioglu and Linder, 2019; Weiss et al., 2013; Mora and Boudaoud, 2006), but also fracture (Plummer et al., 2024; Leslie et al., 2021; VanZanten et al., 2024). Polyethylene glycol (PEG) gels are inherently brittle and prone to fracture, which limits their use for high-toughness applications. However, their biocompatibility and tunable network structure make them well-suited for controlled drug delivery (Qiu and Park, 2001; Wang et al., 2023). To advance this application, de Silva and Lapitsky (2016) proposed a design principle for self-rupturing gels that release drugs at designated times by combining two gels with different swelling ratios. Moreover, rupture can also occur in a homogeneous gel under obstruction or nonuniform swelling. Plummer et al. (2024) demonstrated that hydrogels can break when their swelling is mechanically obstructed. Moreover, recent studies indicate that fracture can occur even under less-constrained conditions, offering valuable insights to the design of self-rupturing gels for drug delivery (Leslie et al., 2021; VanZanten et al., 2024). Collectively, these studies motivate the development of predictive models that couple solvent transport to fracture initiation and propagation.

Fracture models can be categorized into discontinuous and continuous approaches. Typical discontinuous methods are the cohesive

* Corresponding author.
E-mail address: g-buscarnera@northwestern.edu (G. Buscarnera).

https://doi.org/10.1016/j.ijsolstr.2026.114220
Received 21 October 2025; Received in revised form 9 July 2026; Accepted 14 July 2026
Available online 18 July 2026

zone model (Barenblatt, 1959, 1962) and the extended finite element method (XFEM) (Moës et al., 1999). When discontinuous approaches are adopted, a strong discontinuity is introduced in the displacement field. Due to the challenges of handling discontinuities, continuous approaches are more effective in capturing the evolution of crack topologies and addressing multiphysical problems. An increasingly used continuum-scale approach is the phase-field model (PFM), which treats discontinuity as one phase-field parameter encompassing complex crack topologies. Francfort and Marigo (1998) used a variational approach to extend Griffith's theory to include the crack initiation, which provides the baseline for the phase-field model. Later, Bourdin et al. (2000) provided the numerical implementation of the previous model. Kuhn and Müller (2008, 2010) introduced the term phase-field which is a concept employed in physics and materials science to distinguish between different states or phases. Subsequently, a history field has been introduced to ensure irreversibility and further popularized the method (Miehe et al., 2010a,b). A key strength of the phase-field approach is its inherent continuity, which makes it particularly well suited to multiphysics problems. It has been used to simulate hydraulic fracture (Miehe et al., 2015a; Yuan et al., 2025), thermal fracture (Miehe et al., 2015b), and hydrogel fracture under mechanical loading (Zheng et al., 2022). However, many swelling-induced fracture studies are focused on pre-existing cracks (Noselli et al., 2016; Yu et al., 2018) but the underlying mechanisms of crack initiation are not fully understood during not only swelling but also drying. For instance, Böger et al. (2017) introduced a phase-field model to simulate drying-induced fracture with crack initiation and propagation, yet their prediction diverges from the fracture patterns observed by the experiments (Chung et al., 2016).

Our work aims to investigate why polymer gels undergo swelling-induced fracture and further identify dimensionless control parameters for self-rupture behavior. First, we adopt the chemoelastic framework from Anand (2015) by calibrating it with experimental data. Then this model is extended to include a phase-field formulation to capture crack initiation and growth during swelling. A dimensionless analysis is carried out to find the control parameters. The size effect of the brittle polymer gel is also experimentally verified and the corresponding material toughness is determined. The threshold between diffuse swelling and self-rupture response is obtained by systematically scanning the dimensionless parameter space using the proposed model. Thus, our work demonstrates that by adjusting network properties such as crosslinking density and chain length, engineers can control the self-rupture behavior of brittle polymer gels.

2. Chemoelasticity

This section presents a chemoelasticity model used in this study. Anand (2015) demonstrates that linear poroelasticity emerges as a special case of the more general chemoelasticity framework. While a nonlinear framework is generally required for large deformations of gels, a linear theory can still be used for analytical analysis (Yu et al., 2018).

2.1. Balance laws

For the mechanical equilibrium, the following equation can be formulated when the process is assumed to be quasi-static

$$\nabla \cdot \boldsymbol{\sigma} + \boldsymbol{b} = \boldsymbol{0} \qquad \text{in } \Omega \tag{1a}$$

$$\boldsymbol{u} = \boldsymbol{u}_b \qquad \text{on } \partial\Omega_{Du} \tag{1b}$$

$$\boldsymbol{\sigma} \cdot \boldsymbol{n} = \boldsymbol{t} \qquad \text{on } \partial\Omega_{Nu} \tag{1c}$$

where $\boldsymbol{\sigma}$ is the Cauchy stress tensor, $\boldsymbol{b}$ is the body force per unit volume, $\boldsymbol{u}$ is the displacement vector, and $\boldsymbol{n}$ is the outward unit normal vector on the boundary. $\boldsymbol{u}_b$ and $\boldsymbol{t}$ denote the prescribed displacement and traction, respectively. In the swelling problems considered here, the body force is neglected.

Let c denote the solvent concentration, defined as the number of solvent molecules per unit volume, and let $\boldsymbol{j}$ denote the solvent flux vector, defined as the number of solvent molecules crossing a unit area per unit time. In the absence of chemical reactions, the solvent mass balance is written as

$$\dot{c} + \nabla \cdot \boldsymbol{j} = 0 \qquad \text{in } \Omega \tag{2a}$$

$$c = c_b \qquad \text{on } \partial\Omega_{Dc} \tag{2b}$$

$$\boldsymbol{j} \cdot \boldsymbol{n} = i \qquad \text{on } \partial\Omega_{Nc} \tag{2c}$$

where $\dot{c}$ denotes the time derivative of the solvent concentration, c_b is the prescribed concentration, and i is the prescribed normal outward flux.

2.2. The first law and the second law of thermodynamics

We consider an isothermal chemoelastic system characterized by two internal variables $\boldsymbol{\epsilon}$ and c with Helmholtz free-energy density per unit volume $\psi_0(\boldsymbol{\epsilon}, c)$. The system exchanges energy with the surroundings through mechanical work of body forces and tractions, and chemical work associated with solvent flux across the boundary at chemical potential $\mu(\boldsymbol{x}, t)$. In the current description, the rate of change of the total free energy of the system can be written as

$$\dot{\mathcal{G}} = \int_\Omega \dot{\psi}_0 \, d\Omega - \int_\Omega \boldsymbol{b} \cdot \dot{\boldsymbol{u}} \, d\Omega - \int_{\partial\Omega_{Nu}} \boldsymbol{t} \cdot \dot{\boldsymbol{u}} \, d\Gamma + \int_{\partial\Omega_{Nc}} \mu \, i \, d\Gamma \tag{3}$$

For the free-energy density $\psi_0(\boldsymbol{\epsilon}, c)$, the chain rule gives

$$\dot{\psi}_0 = \frac{\partial \psi_0}{\partial \boldsymbol{\epsilon}} : \dot{\boldsymbol{\epsilon}} + \frac{\partial \psi_0}{\partial c} \dot{c} \tag{4}$$

By combining the momentum balance, the solvent mass balance, and the divergence theorem, the following can be obtained

$$\dot{\mathcal{G}} = \int_\Omega \left(\frac{\partial \psi_0}{\partial \boldsymbol{\epsilon}} - \boldsymbol{\sigma} \right) : \dot{\boldsymbol{\epsilon}} \, d\Omega - \int_{\partial\Omega_{Nc}} \left(\frac{\partial \psi_0}{\partial c} - \mu \right) i \, d\Gamma + \int_\Omega \boldsymbol{j} \cdot \nabla \left(\frac{\partial \psi_0}{\partial c} \right) d\Omega \tag{5}$$

For an isothermal process, the second law requires that the free energy of the system never increases, i.e., $\dot{\mathcal{G}} \leq 0$. It is assumed that local rearrangement of molecules and exchange between each pump and the nearby body are fast, so that they are treated as locally equilibrated. Under these local equilibrium assumptions, the first and second terms in Eq. (5) must vanish for arbitrary $\dot{\boldsymbol{\epsilon}}$ and i, yielding the equations of state

$$\boldsymbol{\sigma} = \frac{\partial \psi_0(\boldsymbol{\epsilon}, c)}{\partial \boldsymbol{\epsilon}} \tag{6a}$$

$$\mu = \frac{\partial \psi_0(\boldsymbol{\epsilon}, c)}{\partial c} \tag{6b}$$

2.3. Conduction laws

Diffusion-mechanics coupling is considered as the main mechanism for the time-dependent swelling kinetics (Tanaka and Fillmore, 1979). Assuming the material is isotropic, the diffusion flux is (Zhang and Zhong, 2017)

$$\boldsymbol{j} = -\frac{D c_R}{k_b T} \nabla \mu \tag{7}$$

where D is the diffusivity, c_R is the reference concentration of the diffusing species, k_b is Boltzmann constant, T is the absolute temperature, μ is the chemical potential.

This ensures the dissipation term is always non-negative

$$\boldsymbol{\Phi}_C = -\boldsymbol{j} \cdot \nabla \left(\frac{\partial \psi_0}{\partial c} \right) = \nabla \mu \cdot \frac{D c_R}{k_b T} \nabla \mu \geq 0 \tag{8}$$

2.4. Constitutive laws

Following the Helmholtz free energy density in Anand (2015) and applying $\boldsymbol{\sigma} = \partial\psi_0/\partial\boldsymbol{\epsilon}$ and $\mu = \partial\psi_0/\partial c$, then the constitutive relations can be obtained

$$\psi_0(\boldsymbol{\epsilon}, c) = \frac{\lambda}{2}\left(\mathrm{tr}\,\boldsymbol{\epsilon}\right)^2 + G\,\boldsymbol{\epsilon} : \boldsymbol{\epsilon} + r(c - c_0)\,\mathrm{tr}\,\boldsymbol{\epsilon} + \mu_0(c - c_0) + \frac{g}{2}(c - c_0)^2 \quad (9a)$$

$$\boldsymbol{\sigma} = 2G\boldsymbol{\epsilon} + \{\lambda \mathrm{tr}(\boldsymbol{\epsilon}) + r(c - c_0)\}\boldsymbol{I} \quad (9b)$$

$$\mu - \mu_0 = r\,\mathrm{tr}(\boldsymbol{\epsilon}) + g(c - c_0) \quad (9c)$$

where λ is the Lamé constant, G is the shear modulus, r is stress-chemical coefficient which measures the effect of concentration change on stress or the effect of strain on the chemical potential, $r = -\beta(2G + 3\lambda)$, β is the chemical dilation coefficient which measures the expansion by diffusion, and g represents the scalar chemistry modulus which measures the contribution of concentration change to the chemical potential change, c_0 is the initial concentration of the diffusing species and μ_0 is the initial chemical potential.

2.5. Weak form

The weak form is formulated according to the above governing equations and then is discretized and solved via finite element method. The constitutive relations at each time step can be discretized in time

$$\dot{\mu} = r\,\mathrm{tr}(\dot{\boldsymbol{\epsilon}}) + g\dot{c} \quad (10)$$

The implicit Euler scheme is used to calculate the time derivative and the Eq. (10) can be written in the following form using Eq. (2a).

$$\frac{\mu^n - \mu^{n-1}}{\Delta t} - r\,\mathrm{tr}\left(\frac{\boldsymbol{\epsilon}^n - \boldsymbol{\epsilon}^{n-1}}{\Delta t}\right) = \frac{gDc_R}{k_bT}\nabla^2\mu^n \quad \text{in} \quad \Omega \quad (11a)$$

$$\mu^n = \mu_b \quad \text{on} \quad \partial\Omega_{D\mu} \quad (11b)$$

$$\boldsymbol{j}\cdot\boldsymbol{n} = i \quad \text{on} \quad \partial\Omega_{N\mu} \quad (11c)$$

where μ^n and ϵ^n are the unknown variables to be solved while μ^{n-1} and ϵ^{n-1} represent the variable at the previous step.

In the numerical implementation, the chemical potential μ is used as the primary diffusion unknown using Eq. (9c). The weak form of the chemoelasticity model can be formulated as

$$R_\mu = \int_\Omega \left[\frac{\mu^n - \mu^{n-1}}{\Delta t} - r\,\mathrm{tr}\left(\frac{\boldsymbol{\epsilon}^n - \boldsymbol{\epsilon}^{n-1}}{\Delta t}\right)\right]\delta\mu\,d\Omega + \int_\Omega \frac{gDc_R}{k_bT}\nabla\mu^n\cdot\nabla\delta\mu\,d\Omega + \int_{\partial\Omega_{N\mu}} gi\,\delta\mu\,d\Gamma = 0 \quad (12a)$$

$$R_u = \int_\Omega \left\{2G\boldsymbol{\epsilon}^n + \left[\lambda\mathrm{tr}(\boldsymbol{\epsilon}^n) + \frac{r}{g}(\mu^n - \mu_0 - r\,\mathrm{tr}(\boldsymbol{\epsilon}^n))\right]\boldsymbol{I}\right\} : \nabla\delta\boldsymbol{u}\,d\Omega - \int_\Omega \boldsymbol{b}\cdot\delta\boldsymbol{u}\,d\Omega - \int_{\partial\Omega_{Nu}} \boldsymbol{t}\cdot\delta\boldsymbol{u}\,d\Gamma = 0 \quad (12b)$$

3. Chemoelastic phase-field model

3.1. Rate variational formulation and phase field approximation

The Helmholtz free-energy density $\psi_0(\boldsymbol{\epsilon}, c)$ can be reorganized as

$$\psi_0(\boldsymbol{\epsilon}, c) = \frac{1}{2}K\left[\mathrm{tr}(\boldsymbol{\epsilon}) + \frac{r}{K}(c - c_0)\right]^2 + G\,\boldsymbol{\epsilon}^d : \boldsymbol{\epsilon}^d + \mu_0(c - c_0) + \frac{1}{2}\left(g - \frac{r^2}{K}\right)(c - c_0)^2 \quad (13)$$

In this section, a rate variational formulation is developed to determine the governing equations of the coupled problem including fracture which is an extension of Section 2. Following Miehe et al. (2014), the rate-variational formulation of a multi-field dissipative problem can be written in terms of a continuous rate potential of the form

$$\dot{\Pi} = \dot{\mathcal{E}} + \mathcal{D} - \dot{\mathcal{P}} \quad (14)$$

where $\dot{\mathcal{E}}$ is the rate of the energy storage functional, $\mathcal{D}$ is the dissipation potential functional, and $\dot{\mathcal{P}}$ is the external power functional.

In this study, the rate potential contains the rate of stored chemoelastic and fracture energy, the extended dissipation potential caused by solvent transport, and external power:

$$\dot{\Pi}(\dot{\boldsymbol{u}}, \dot{c}, \mu, \dot{\Gamma}_c) = \frac{d}{dt}\int_\Omega \psi_0(\boldsymbol{\epsilon}(\boldsymbol{u}), c)\,d\Omega + \frac{d}{dt}\int_{\Gamma_c} G_c\,d\Gamma + \int_\Omega\left[-\mu\dot{c} - \frac{1}{2}M\nabla\mu\cdot\nabla\mu\right]d\Omega - \int_\Omega \boldsymbol{b}\cdot\dot{\boldsymbol{u}}\,d\Omega - \int_{\partial\Omega_{N_u}} \boldsymbol{t}\cdot\dot{\boldsymbol{u}}\,d\Gamma - \int_{\partial\Omega_{N\mu}} \mu i\,d\Gamma \quad (15)$$

where G_c is the material toughness, and M is the solvent mobility which is defined as $M = c_R D/k_bT$. Note that the external chemical boundary term appears with a negative sign in the rate potential, whereas the chemical power is added in the thermodynamic balance. This is a mathematically necessary consequence of the saddle-point nature of the mixed variational formulation, ensuring that the stationarity conditions yield the correct positive constitutive relation. The crack is treated as permeable to solvent transport. Consequently, no additional solvent source or flux is assigned to the crack surface, and the chemical potential is assumed to remain continuous across the regularized crack. Bourdin et al. (2000) proposed a volumetric approximation to the crack surface integral for numerical treatment by introducing the phase-field variable d, where $d = 0$ indicates the pristine state of the material and $d = 1$ indicates a fully broken state. Using the phase-field variable, the crack surface integral can be approximated by a volume integral:

$$\int_{\Gamma_c} G_c\,d\Gamma \approx \int_\Omega G_c\gamma(d, \nabla d)\,d\Omega \quad (16)$$

The AT-2 type regularized crack surface density is defined as

$$\gamma(d, \nabla d) = \frac{1}{2l}d^2 + \frac{l}{2}|\nabla d|^2 \quad (17)$$

where l is the length-scale parameter that controls the width of the regularized crack.

The damaged free energy is assumed to take the following form:

$$\psi(\boldsymbol{\epsilon}, c, d) = g_d(d)\psi_+(\boldsymbol{\epsilon}, c) + \psi_-(\boldsymbol{\epsilon}, c) \quad (18)$$

with $g_d(d) = (1 - d)^2$. In the present formulation, damage degrades the crack-driving chemomechanical part of the free energy, while solvent transport is not degraded by the phase-field variable. Similar to Luo et al. (2023), the effective volumetric strain is introduced inside the tensile-compressive split, leading to the following energy decomposition:

$$\psi_+ = \frac{K}{2}\left\langle \mathrm{tr}(\boldsymbol{\epsilon}) + \frac{r}{K}(c - c_0)\right\rangle_+^2 \quad (19a)$$

$$\psi_- = \frac{K}{2}\left\langle \mathrm{tr}(\boldsymbol{\epsilon}) + \frac{r}{K}(c - c_0)\right\rangle_-^2 + G\,\boldsymbol{\epsilon}^d : \boldsymbol{\epsilon}^d + \mu_0(c - c_0) + \frac{1}{2}\left(g - \frac{r^2}{K}\right)(c - c_0)^2 \quad (19b)$$

Here, $\langle x\rangle_\pm := (x \pm |x|)/2$, and $\boldsymbol{\epsilon}^d = \boldsymbol{\epsilon} - \frac{1}{3}\mathrm{tr}(\boldsymbol{\epsilon})\boldsymbol{I}$. This decomposition satisfies $\psi_+ + \psi_- = \psi_0$, where ψ_0 is the undamaged free-energy density. In the present formulation, ψ_+ contains only the tensile volumetric contribution and therefore represents the crack-driving part degraded by $g_d(d)$. This energy split is adopted as a mode-I-oriented approximation for the PEG-based gels studied here, whose fracture response is dominated by tensile opening. Here, G_c is taken to scale with the mode-I fracture energy G_{Ic}.

Substituting the regularized crack surface energy and the damaged chemoelastic free-energy density into Eq. (15) gives the following phase-field approximation of the proposed variational statement:

$$\begin{aligned}\dot{\Pi}(\dot{\boldsymbol{u}},\dot{c},\mu,\dot{d}) = &\frac{d}{dt}\int_\Omega \psi(\boldsymbol{\epsilon}(\boldsymbol{u}),c,d)\,d\Omega + \frac{d}{dt}\int_\Omega G_c\gamma(d,\nabla d)d\Omega \\ &+ \int_\Omega \left[-\mu\dot{c} - \frac{1}{2}M\nabla\mu\cdot\nabla\mu\right] d\Omega \\ &- \int_\Omega \boldsymbol{b}\cdot\dot{\boldsymbol{u}}\,d\Omega - \int_{\partial\Omega_{N_u}} \boldsymbol{t}\cdot\dot{\boldsymbol{u}}\,d\Gamma - \int_{\partial\Omega_{N\mu}} \mu i\,d\Gamma\end{aligned} \tag{20}$$

3.2. Strong form

The governing equations for the coupled problem in this study are obtained from the stationarity conditions of the rate potential $\dot{\Pi}$ in Eq. (20), together with the chemoelastic constitutive relations under permeable crack assumption

$$\dot{\mu} - r\,\mathrm{tr}(\dot{\boldsymbol{\epsilon}}) - \frac{gDc_R}{k_bT}\nabla^2\mu = 0 \qquad \text{in } \Omega \tag{21a}$$

$$\nabla\cdot\boldsymbol{\sigma}(\boldsymbol{\epsilon},c,d) + \boldsymbol{b} = 0 \qquad \text{in } \Omega \tag{21b}$$

$$\frac{G_c}{l}\left(d - l^2\nabla^2 d\right) = 2(1-d)\psi_+ \qquad \text{in } \Omega \tag{21c}$$

$$\nabla d\cdot\boldsymbol{n} = 0 \qquad \text{on } \partial\Omega_{Nd} \tag{21d}$$

$$\boldsymbol{u} = \boldsymbol{u}_b \qquad \text{on } \partial\Omega_{Du} \tag{21e}$$

$$\boldsymbol{\sigma}\cdot\boldsymbol{n} = \boldsymbol{t} \qquad \text{on } \partial\Omega_{Nu} \tag{21f}$$

$$\mu = \mu_b \qquad \text{on } \partial\Omega_{D\mu} \tag{21g}$$

$$\boldsymbol{j}\cdot\boldsymbol{n} = i \qquad \text{on } \partial\Omega_{N\mu} \tag{21h}$$

where $\boldsymbol{\sigma}(\boldsymbol{\epsilon},c,d) = \partial\psi(\boldsymbol{\epsilon},c,d)/\partial\boldsymbol{\epsilon}$.

A local history field $\mathcal{H}$ is used to record the maximum local free energy ψ_+ in history to ensure the process irreversible (Miehe et al., 2015b; Xue et al., 2021), so that

$$\frac{G_c}{l}(d - l^2\nabla^2 d) = 2(1-d)\mathcal{H} \tag{22a}$$

$$\mathcal{H}(\boldsymbol{x},t) = \max_{s\in[0,t]}\psi_+(\boldsymbol{x},s) \tag{22b}$$

3.3. Weak form and numerical implementation

The weak form of the chemoelastic phase-field model is shown below:

$$\begin{aligned}R_\mu = &\int_\Omega [\frac{\mu^n - \mu^{n-1}}{\Delta t} - r\,\mathrm{tr}(\frac{\boldsymbol{\epsilon}^n - \boldsymbol{\epsilon}^{n-1}}{\Delta t})]\delta\mu d\Omega \\ &+ \int_\Omega \frac{gDc_R}{k_bT}\nabla\mu^n\cdot\nabla\delta\mu d\Omega + \int_{\partial\Omega_{N\mu}} gi\,\delta\mu\,d\Gamma = 0\end{aligned} \tag{23a}$$

$$R_u = \int_\Omega \boldsymbol{\sigma}(\boldsymbol{\epsilon},c,d) : \nabla\delta\boldsymbol{u}d\Omega - \int_\Omega \boldsymbol{b}\cdot\delta\boldsymbol{u}\,d\Omega - \int_{\partial\Omega_{Nu}} \boldsymbol{t}\cdot\delta\boldsymbol{u}\,d\Gamma = 0 \tag{23b}$$

$$R_d = G_c\int_\Omega (\frac{d}{l}\delta d + l\nabla d\cdot\nabla\delta d)d\Omega - \int_\Omega [2\mathcal{H}(1-d)\delta d]d\Omega = 0 \tag{23c}$$

These equations can be solved in a staggered scheme (Miehe et al., 2010a; Choo and Sun, 2018; Wilson et al., 2013). First, the chemomechanical problem is solved using Eqs. (23a) and (23b) simultaneously when the damage variable d is fixed. Then Eq. (23c) is used to determine the damage variable d when the displacement $\boldsymbol{u}$ and chemical field c are fixed. The flowchart of this staggered scheme is shown in Fig. 1. For simplicity, the diffusion coefficient D is assumed constant throughout the domain, including damaged regions. This is a modeling simplification motivated by the short rupture duration considered here and by the absence of a well-established constitutive dependence of D on damage (Mao and Anand, 2018). The whole process is solved using the open-source code JAX-FEM developed by Xue et al. (2023).

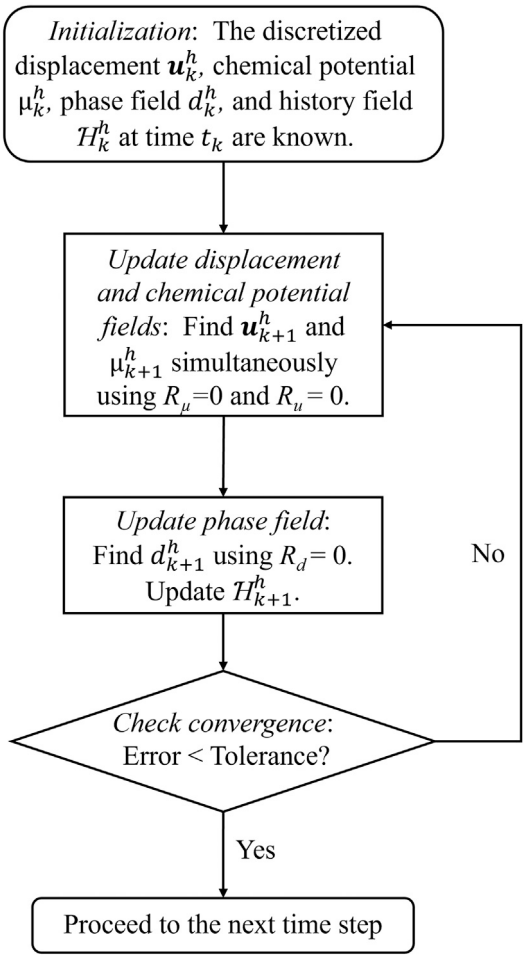

Fig. 1. Staggered scheme for the chemoelastic phase-field model at time step $[t_k, t_{k+1}]$.

4. Dimensional analysis

This section derives the dimensionless parameters from the governing equations for the undamaged material together with the size-effect law. Therefore, the following derivation is performed without the phase-field approximation. By combining the conservation laws (Eqs. (1a) and (2a)) and constitutive relations (Eqs. (9b) and (9c)), the following two governing equations can be obtained:

$$2G\nabla\cdot\boldsymbol{\epsilon} + \lambda\nabla\mathrm{tr}(\boldsymbol{\epsilon}) + r\nabla c = 0 \tag{24a}$$

$$\frac{\partial c}{\partial t} - \frac{rDc_R}{k_bT}\nabla^2\mathrm{tr}(\boldsymbol{\epsilon}) - \frac{gDc_R}{k_bT}\nabla^2 c = 0 \tag{24b}$$

A new coordinate is chosen as $\nabla_\xi = h\nabla$ and dimensionless time $\tau = c_R g Dt/(k_bTh^2)$ where h is the thickness of the sample. The diffusion length is proportional to $\sqrt{Dt}$ (Bird et al., 2006). Therefore, diffusion along the thickness direction is considered dominant if it is significantly smaller than other dimensions. Moreover, in this analysis the samples remain geometrically similar regardless of size. The nondimensional governing equations are given by

$$2\nabla_\xi\cdot\boldsymbol{\epsilon} + \frac{\lambda}{G}\nabla_\xi\mathrm{tr}(\boldsymbol{\epsilon}) + \frac{rc_R}{G}\nabla_\xi\frac{c}{c_R} = 0 \tag{25a}$$

$$\frac{\partial\frac{c}{c_R}}{\partial\tau} - \frac{r}{gc_R}\nabla_\xi^2\mathrm{tr}(\boldsymbol{\epsilon}) - \nabla_\xi^2\frac{c}{c_R} = 0 \tag{25b}$$

Thus, the dimensionless parameters of the two governing equations are $\frac{\lambda}{G}$, $\frac{rc_R}{G}$, and $\frac{r}{gc_R}$.

Table 1
The meaning of the proposed dimensionless control parameters for swelling–induced fracture.

Dimensionless parameters	Physical meaning
Gh/G_{Ic}	Competition between load caused by eigenstrain and fracture resistance.
λ/G	The volumetric compressibility of the sample.
βc_R	The normalized swelling ratio of the sample.
$G/(g c_R^2)$	The competition between mechanical stiffness and chemical stiffness which shows how strongly μ responds to c.

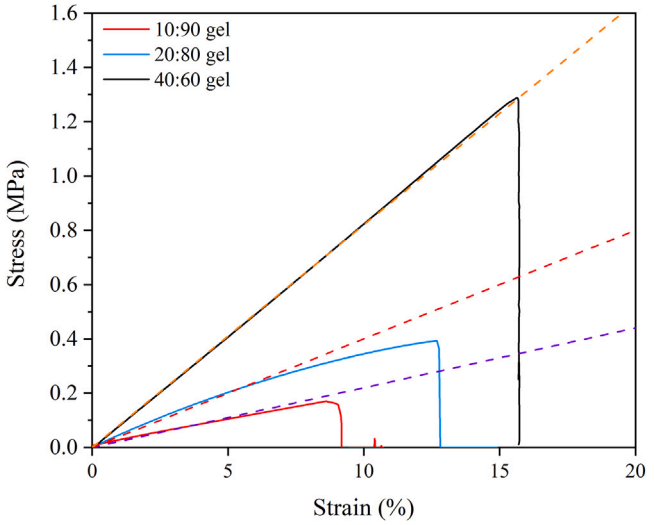

Fig. 2. The uniaxial test results of 10:90, 20:80, and 40:60 gels.

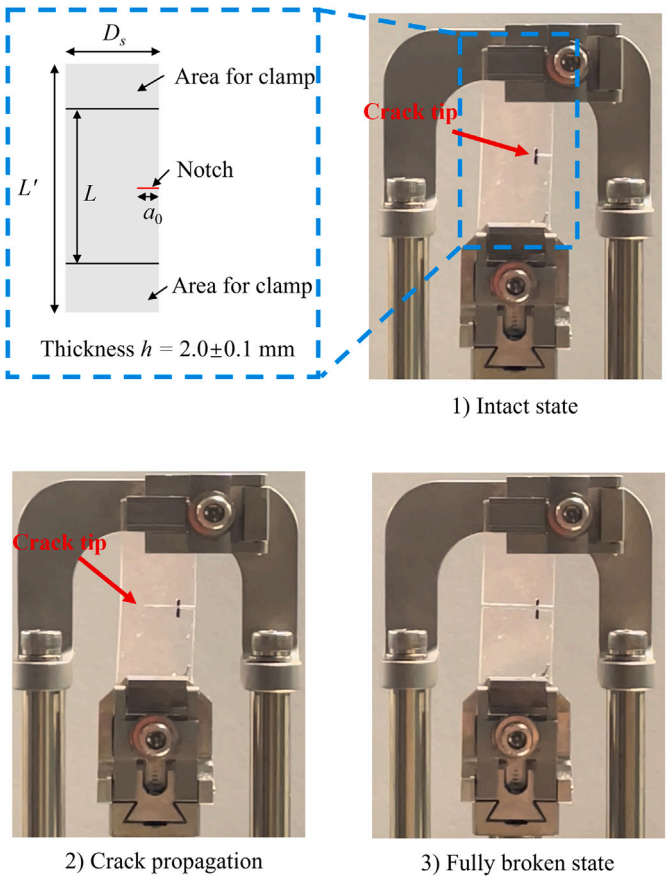

Fig. 3. The sample with a single-edge notch under uniaxial tension.

The dimensionless stress can then be expressed using these parameters:

$$\frac{\boldsymbol{\sigma}}{G} = 2\epsilon + \{\frac{\lambda}{G}\mathrm{tr}(\epsilon) + \frac{rc_R}{G}\frac{c-c_0}{c_R}\}\boldsymbol{I} \tag{26}$$

As we only consider the isotropic swelling, the mean stress can be expressed as:

$$\sigma_m = Gf(\frac{\lambda}{G}, \frac{rc_R}{G}, \frac{r}{gc_R}) \tag{27}$$

Here, the dimensional analysis of size effect on fracture behavior is adopted (Bazant et al., 2021) and then the following equation can be obtained by applying Irwin's relation ($K_{Ic}^2 = EG_{Ic}$):

$$\Psi(\sigma_m\sqrt{\frac{h}{EG_{Ic}}}, \frac{h}{D_s}, \frac{L}{D_s}, \frac{a_0}{D_s}) = 0 \tag{28}$$

where h, L and D_s are the sample's thickness, length, and width.

If we keep the sample geometrically similar (h/D_s and L/D_s), then the dimensionless parameters for the same fracture pattern (a_0/D_s) are:

$$\sigma_m\sqrt{\frac{h}{EG_{Ic}}} = \sqrt{\frac{Gh}{G_{Ic}}}\Phi(\frac{\lambda}{G}, \beta c_R, \frac{G}{gc_R^2}) \tag{29}$$

Therefore, by nondimensionalizing the constitutive equations, we have identified the four nondimensional control parameters in the system:

$$\frac{Gh}{G_{Ic}}, \frac{\lambda}{G}, \beta c_R, \frac{G}{gc_R^2} \tag{30}$$

The meaning of these four dimensionless parameters is shown in Table 1.

5. Results and discussion

5.1. Measuring the toughness of PEG-based polymer gel using size effect law

Polymer gel samples with three formulations were prepared by mixing polyethylene glycol diacrylate (PEGDA) (average molecular weight M_n = 700 g/mol) with polyethylene glycol methyl ether acrylate (PEGMEA) at mole ratios of 10:90, 20:80, and 40:60. For simplicity, these formulations will be referred to as the 10:90, 20:80, and 40:60 gels later in this work. The details of sample preparation can be found in VanZanten et al. (2024). Initially, three intact samples were tested under uniaxial tension and the results are shown in Fig. 2. The stiffness and strength of the sample increase with increasing PEGDA ratio since PEGDA works as the crosslinker in the system (Levin et al., 2024). The result also verifies that the linear and small strain assumptions are appropriate for modeling these PEG-based polymer gels. Additionally, notched samples were used to verify the size effect law. The geometry of the single-edge notched sample is shown in Fig. 3. Fig. 3 also shows the process of crack propagation during the test. When the sample is loaded in tension, the initial crack begins to propagate across the sample width until complete failure occurs. The result additionally verifies that the PEG-based gels fail at small deformations, showing the applicability of linear elastic fracture mechanics (LEFM) in this gel. For comparison, a more versatile size effect law for quasi-brittle solids is also used to assess the performance of LEFM in our system. This size effect relation is given by Bazant et al. (2021):

$$\sigma_N = Bf_u(1 + D_s/D_0)^{-\frac{1}{2}} = (\frac{EG_{Ic}}{g'(\alpha_0)c_f + g(\alpha_0)D_s})^{\frac{1}{2}} \tag{31}$$

where $\sigma_N = P/(hD_s)$, maximum load P, B is a constant characterizing the solution according to plastic limit analysis based on the

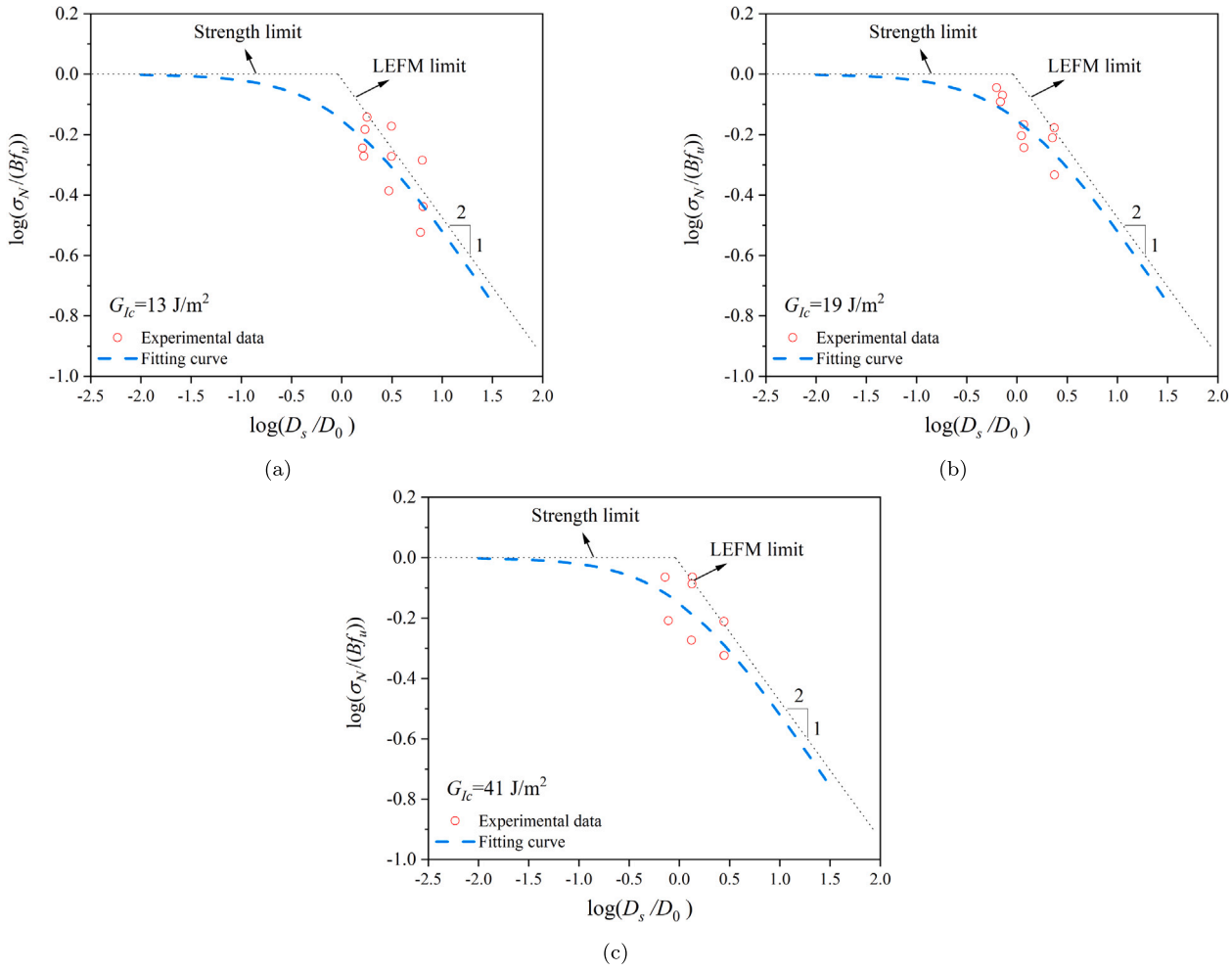

Fig. 4. Toughness measured for: (a) 10:90, (b) 20:80, and (c) 40:60 gels with single-edge notches.

strength concept, f_u is the reference material strength, introduced to make constant B dimensionless, D_0 is the constant depending on both fracture process zone size and specimen geometry, c_f is a length scale representing the effective length of the fracture process zone. $\alpha_0 = a_0/D_s = 0.2$ where a_0 is the initial length of the notch. Here, $g(\alpha) = \pi\alpha[F(\alpha)]^2$ where $F(\alpha)$ can be obtained from Tada et al. (1973). For the single-edge notched specimens, $g(\alpha)$ and $g'(\alpha)$ are

$$g(\alpha) = \pi\alpha[1.122 - 0.231\alpha + 10.55\alpha^2 - 21.71\alpha^3 + 30.38\alpha^4]^2 \tag{32a}$$

$$g'(\alpha) = \pi[1.259 - 1.037\alpha + 71.18\alpha^2 - 214.4\alpha^3 + 947.5\alpha^4] \tag{32b}$$

The material toughness can therefore be obtained by

$$G_{Ic} = \frac{(Bf_u)^2}{E} D_0 g(\alpha_0) \tag{33}$$

The fitting curves of different polymer gels are shown in Fig. 4 using Eq. (31). While LEFM offers a first-order depiction of the fracture behavior of brittle polymer gels, the superior performance of the size effect law in Eq. (31) indicates that this expression is satisfactory for this class of materials. Moreover, the toughness G_{Ic} of different gels can be obtained using Eq. (33), with the corresponding values being reported in Fig. 4. The results indicate that the crosslinking density of the polymer not only increases material stiffness and strength but also toughness. The polymer chain length is another critical factor that strongly influences the material's mechanical properties. Existing studies show that longer chains reduce stiffness but enhance toughness (Pruksawan et al., 2023; Anindita et al., 2023; Bhattacharya and Shunmugam, 2020). A deeper understanding of the relation between polymer compositions and mechanical properties will improve the design of polymer systems.

5.2. Modeling of diffusion induced swelling

In this section, experimental swelling data are used to calibrate the model described in Section 2. Since the sample thickness is small compared to sample width and length, here we only calibrate the two dimensional cross section. Exploiting the symmetry of the system, we simulate only one-quarter of the specimen cross-section (5 mm × 1 mm) to reduce computational cost. Fig. 5 shows the deformation of a quarter cross section of gel sample in the simulation and a full cross section gel sample in the experiment. The results reveal that the gradient of eigenstrain is localized near the sample's corners/edges. This gradient of eigenstrain is the driving force of the self-rupture which will be discussed in the next section. Fig. 6(a) shows the stretch λ change over time during swelling, measured experimentally and predicted by simulation. The results show that the linear chemoelasticity framework can capture the swelling data measured in PEG hydrogels. Additionally, the convergence of the solution with respect to mesh size was tested, and only the finest mesh (250 × 50) was selected to compare with the experimental data reported in VanZanten et al. (2024). The in-plane stress measures used in this study are

$$\sigma_m = \frac{\mathrm{tr}(\boldsymbol{\sigma})}{n} \tag{34a}$$

$$\sigma_v = \sqrt{\frac{3}{2}\boldsymbol{\sigma}^{dev} : \boldsymbol{\sigma}^{dev}} \tag{34b}$$

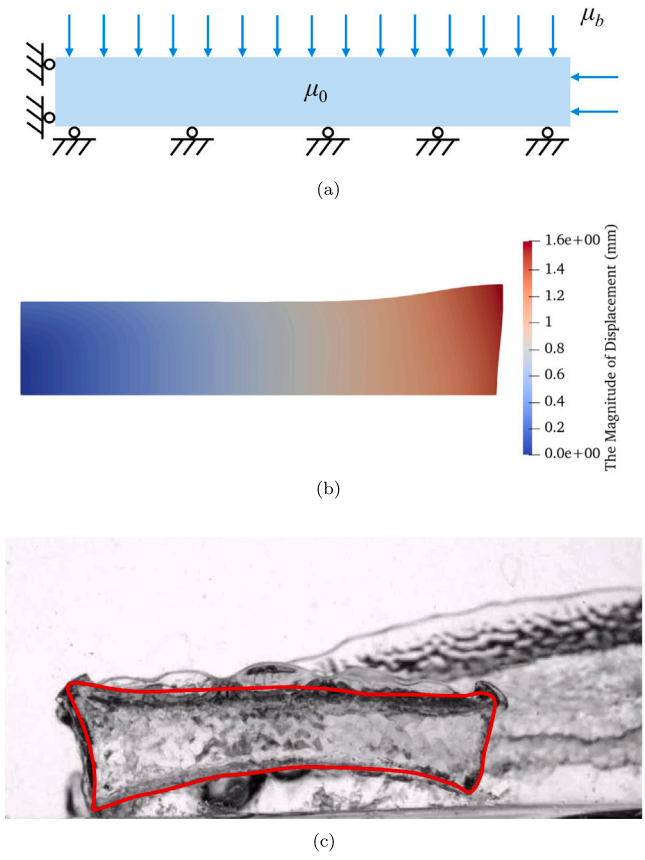

Fig. 5. (a) Schematic of the problem using a quarter cross section; (b) simulated deformation of the gel sample; and (c) experimentally observed deformation of the full cross section of the gel sample.

$$\boldsymbol{\sigma}^{dev} = \boldsymbol{\sigma} - \frac{1}{n}\mathrm{tr}(\boldsymbol{\sigma})\boldsymbol{I} \tag{34c}$$

where n is the dimension of the domain which is 2 here.

Fig. 6(b) shows the stress distribution inside the sample at the early stage of swelling. It indicates that the largest mean stress occurred at the sample corner while the minimum mean stress and maximum von Mises stress appeared at the surface away from the corner. This result shows that the sharp corner will lead to a stress concentration which is also consistent with Steck et al. (2023). The model parameters are listed in Table 2. The Young's modulus of the sample is taken from Leslie et al. (2021) and the Poisson's ratio is measured under uniaxial tension while the remaining parameters are obtained from fitting our swelling measurements. Fig. 7 shows the evolution of stresses during hydrogel swelling and that the calculated stress converges with decreasing mesh sizes. Moreover, both the mean stress and the von Mises stress in the cross-section plane first increase and then decrease throughout the swelling process, eventually converging to zero as equilibrium is reached. Meanwhile, the sample with a higher modulus exhibits a greater stress magnitude, indicating that it generates a greater load during the swelling. However, since the gel resistance also changes with different crosslinking densities and polymer chain lengths, it is unknown which gel is more prone to fracture without a suitable model.

5.3. Modeling of swelling induced fracture

In this section, the simulated domain size is 15 mm × 1.5 mm, which is a quarter of the cross section used in the experiments conducted by Leslie et al. (2021). The element number is chosen as 250 × 50 to ensure accuracy and the length scale parameter is set to the element size for better convergence. Choo et al. (2023) shows that phase-field modeling can capture the energetic size effect law. This law applies not only to concrete and rocks but also to alloys and ceramics, making it a generally applicable principle (Bazant et al., 2021). Fig. 8 shows an example simulation demonstrating that swelling-induced fracture initiation and propagation are observed in our model. The snapshots are recorded sequentially and labeled (a) through (f). Although no initial crack is introduced, the geometry causes stress to concentrate around the sharp corner of the sample. The simulation results indicate that the crack initiates at the corner and propagates into the bulk material. This is similar to the behavior observed in Steck et al. (2023) using the lap shear test. Furthermore, it is shown that the gradient in eigenstrain can drive fracture initiation and subsequent crack propagation. This

Table 2
Model parameters for swelling simulations.

Parameters	10:90 gel	20:80 gel	40:60 gel
Boltzmann constant k_b [mJ/K]		1.381×10^{-20}	
Absolute temperature T [K]		293	
Reference concentration c_R [mm^{-3}]		9.033×10^{15}	
Young's modulus E [MPa]	2.2	5.0	8.7
Poisson's ratio ν [−]	0.25	0.25	0.25
Chemical dilation coefficient β [mm^3]	3.0×10^{-40}	2.6×10^{-40}	1.8×10^{-40}
Chemistry modulus g [mJ mm^3]	5.0×10^{-34}	5.0×10^{-34}	5.0×10^{-34}
Diffusivity D [mm^2/s]	1.0×10^{-4}	7.5×10^{-5}	7.5×10^{-5}

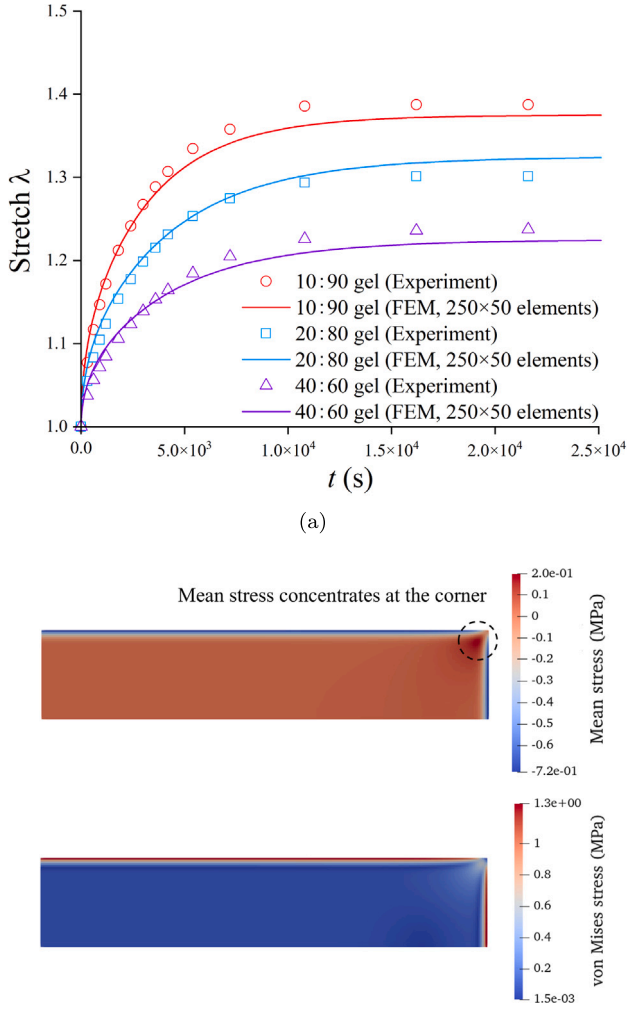

Fig. 6. The simulations of sample swelling: (a) the variations of stretch λ with time t in 10:90, 20:80, and 40:60 gels and (b) stress distribution inside the gel sample.

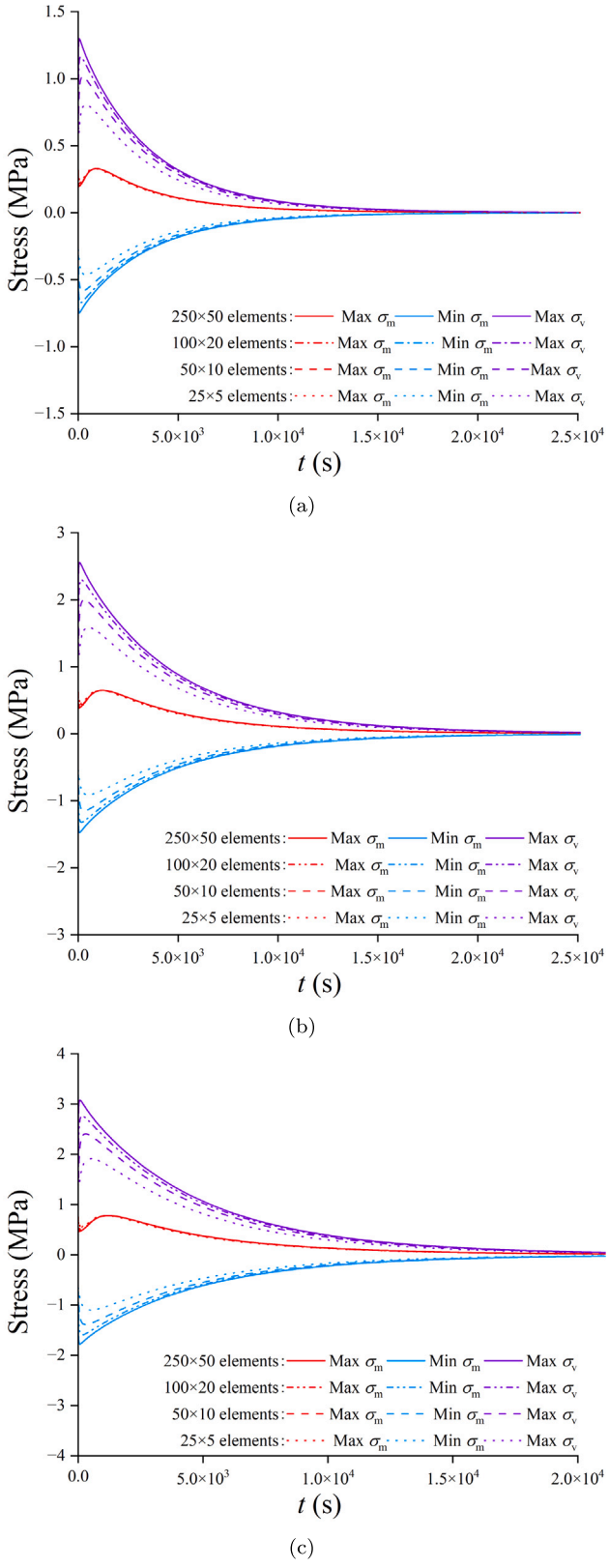

Fig. 7. The variations of stresses with time t of (a) 10:90, (b) 20:80, and (c) 40:60 gels during swelling.

result aligns with experimental observation in Leslie et al. (2021) where cracks typically initiate near the edge of the sample. Fig. 9 displays the evolution of mean stress throughout the swelling process, showing

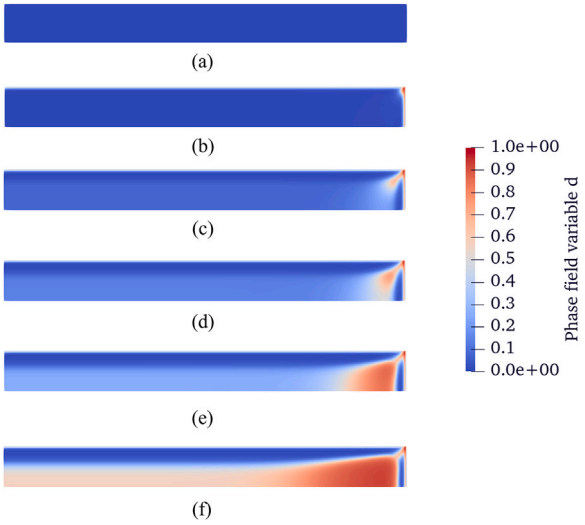

Fig. 8. An example of fracture initiation and propagation.

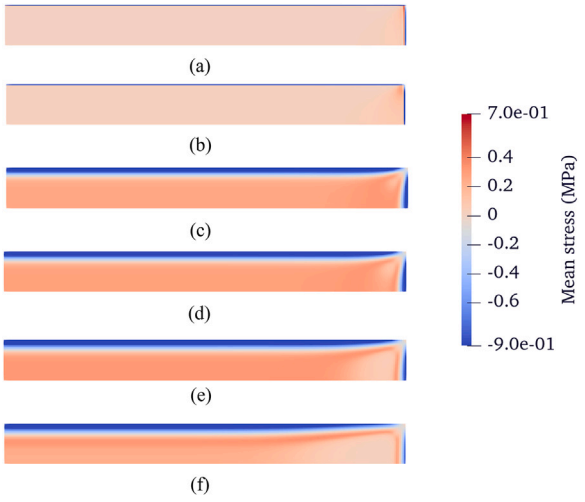

Fig. 9. The evolution of mean stress during swelling.

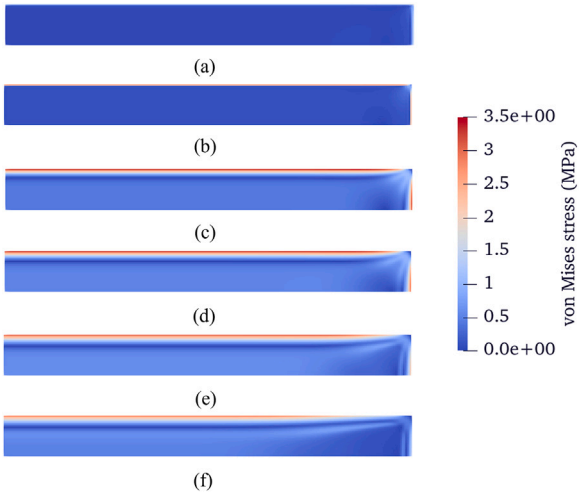

Fig. 10. The evolution of von Mises stress during swelling.

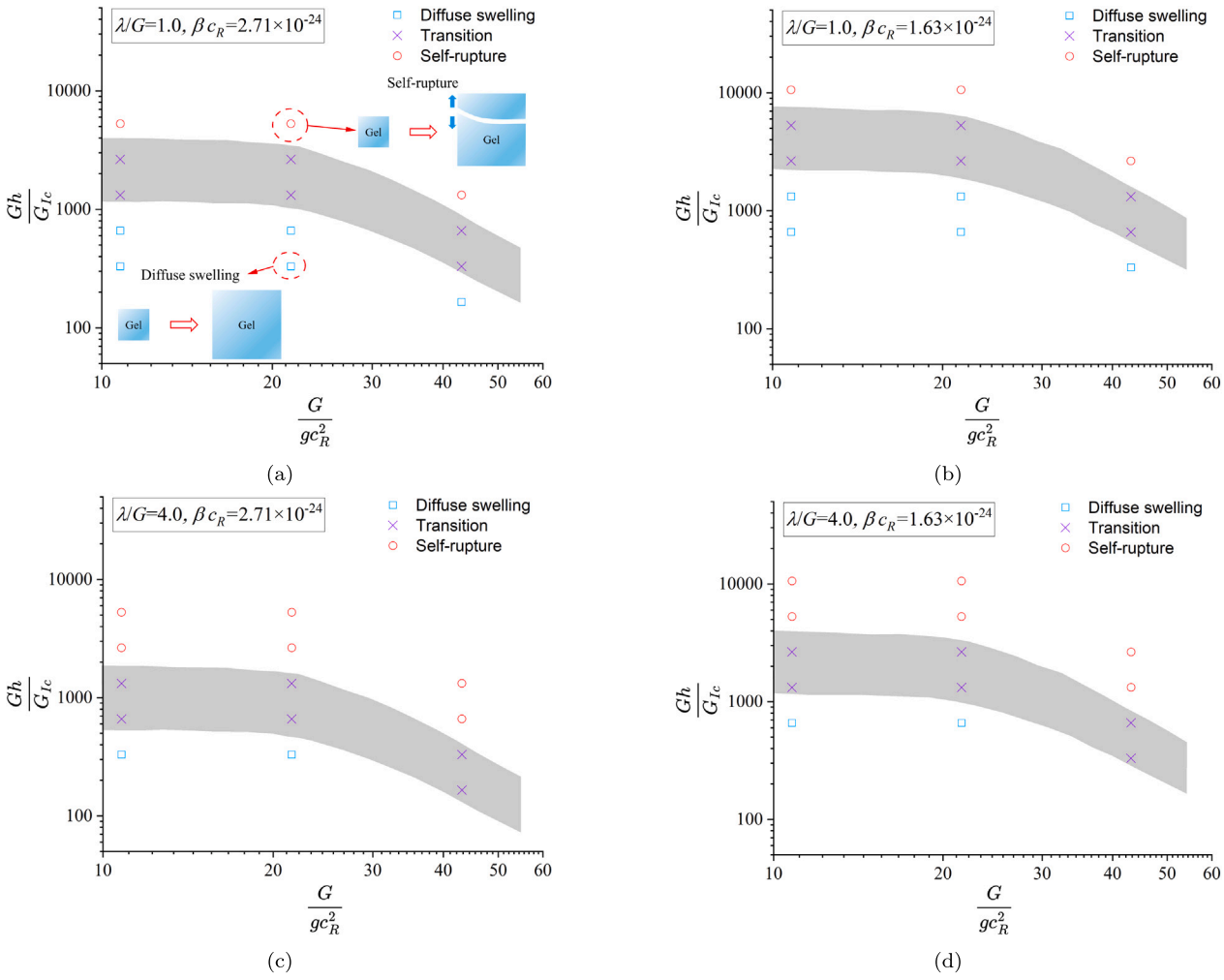

Fig. 11. Design regimes for controlled swelling-induced fracture in brittle polymer gels: (a) $\lambda/G = 1.0$, $\beta c_R = 2.71 \times 10^{-24}$, (b) $\lambda/G = 1.0$, $\beta c_R = 1.63 \times 10^{-24}$, (c) $\lambda/G = 4.0$, $\beta c_R = 2.71 \times 10^{-24}$, and (d) $\lambda/G = 4.0$, $\beta c_R = 1.63 \times 10^{-24}$.

both crack initiation and propagation. Significant stress concentrations appear in Fig. 9(a) and (b) near the sample corner. Following damage, stress inside the damaged region drops, whereas stress in the adjacent material rises. Even though the surface experiences tensile strain, damage is hard to develop there because the eigenstrain is incorporated into the energy decomposition. Additionally, the stress contour indicates that the surface is under compression. This suggests that once both critical thresholds are exceeded, wrinkling or creasing and fracture may occur simultaneously. Fig. 10 illustrates the evolution of von Mises stress during swelling with crack initiation and propagation. The results show that the deviatoric stress at the surface is highest and the stress in the tensile region is the lowest.

Four dimensionless parameters were introduced in Section 4. Fig. 11 shows the design regimes for controlling swelling-induced fracture in brittle polymer gels. With fixed βc_R and λ/G values, different fracture regimes can be found in ($\frac{Gh}{G_{Ic}}$, $\frac{G}{gc_R^2}$) space. As either dimensionless parameter increases in this space, the specimen transitions from the diffuse swelling to the self-rupture regime. In our simulations, the material is considered fractured once the damage variable d exceeds 0.9. Moreover, as the swelling ratio βc_R decreases, the transition boundary shifts up in the dimensionless space. The transition boundary shifts down in the space if λ/G increases. Thus, these results indicate that swelling-induced fracture is predominantly governed by material stiffness and toughness. As stiffness increases or toughness decreases, the material is more likely to cross the fracture transition. To change the dimensionless parameters experimentally, one would change crosslinking density, polymer chain length and any other related physical and chemical properties of brittle polymer gels. Fig. 12 shows a schematic of the possible approaches controlling the self-rupture behavior in brittle polymer gels. Indicated on the figure are experimental observations of how changes in crosslink density and crosslink chain length change the transition from stable swelling to fracture (VanZanten et al., 2024). This analysis highlights that the transition line is primarily influenced by $\frac{Gh}{G_{Ic}}$ and $\frac{G}{gc_R^2}$. Directly quantifying how crosslink density alters the dimensionless control parameters is challenging, in that it is hard to investigate the ratio between the concurrent increases in both stiffness and toughness. However, it is arguable that if the chain length increases, the stiffness decreases and the toughness increases which therefore leads to the shift from self-rupture regime to diffuse swelling regime. Our findings provide guidelines for controlling self-rupture behavior in brittle polymer gels. At the same time, further work is needed to turn these insights into practical design. In particular, the evolution of material toughness during swelling is a crucial component of these processes that still requires proper quantification.

6. Conclusions

This study proposes a chemomechanical phase-field model to investigate the self-rupture of brittle polymer gels under free swelling and define the key control parameters governing their chemo-mechanics. The main conclusions of the study are as follows:

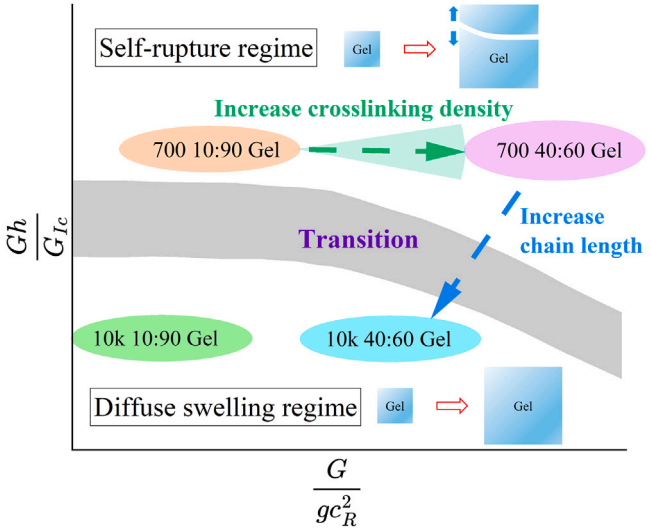

Fig. 12. Schematic of the possible approaches to control the self-rupture behavior in brittle polymer gels. Note: 700 10:90 gel refers to a gel made with PEGDA:PEGMEA ratio of 10:90, where the PEGDA has an average molecular weight of 700 g/mol.

(1) The analysis of uniaxial tension tests on samples with single-edge notches shows that brittle polymer gels fracture in accordance with a size effect law for quasi-brittle solids. It also suggests that their stiffness and toughness increase with increasing crosslinking density.

(2) The proposed chemoelastic phase-field model reproduces the swelling behavior and predicts that cracks nucleate at the specimen's corners before eventually propagating into the bulk. In the examined cases, self-rupture is found to be driven by the gradients of eigenstrain.

(3) Four dimensionless control parameters are identified through a dimensional analysis based on a linearized form of the governing field equations and the size effect law. Systematic exploration of this parameter space delineates a transition between diffuse swelling (i.e., no fracture) and self-rupture. This result sheds light on the underlying mechanics of controlling swelling-induced fracture in brittle soft materials.

By combining measurable material properties, swelling behavior, and fracture resistance into governing dimensionless groups, the present study provides a predictive regime map that can guide the design of polymer gels with controlled self-rupture behavior. These findings also offer new insights for the design of brittle polymer gels with tunable self-rupture behavior, thus facilitating their applications in drug delivery and responsive material applications. However, the present framework is intentionally simple and several extensions can be made in the future. For example, a finite-strain chemoelastic–phase-field formulation would be more appropriate for polymer gels undergoing large deformations. This would involve implementing a hyperelastic free-energy density coupled with swelling (e.g., Flory-Rehner) integrated with the phase-field approximation of the fracture. Additionally, unraveling the evolution of material properties (e.g., stiffness, toughness, and transport parameters) during swelling and damage would allow the model to capture more realistic gel behavior over time.

CRediT authorship contribution statement

Hongwei Wu: Writing – review & editing, Writing – original draft, Validation, Software, Methodology, Data curation, Conceptualization. **Alyssa VanZanten:** Writing – review & editing, Data curation. **Surbhi Punhani-Schillinger:** Writing – review & editing, Data curation. **Samira W. Khan:** Data curation. **Michelle M. Driscoll:** Writing – review & editing, Supervision, Funding acquisition. **Caroline R. Szczepanski:** Writing – review & editing, Supervision, Resources, Funding acquisition. **Giuseppe Buscarnera:** Writing – review & editing, Validation, Supervision, Methodology, Funding acquisition, Conceptualization.

Declaration of competing interest

The authors declare that they have no known competing financial interests or personal relationships that could have appeared to influence the work reported in this paper.

Acknowledgments

This work is supported by the National Science Foundation (DMR-2311697 and DMR-2311698).

Data availability

Data will be made available on request.

References

Anand, L., 2015. 2014 Drucker medal paper: A derivation of the theory of linear poroelasticity from chemoelasticity. J. Appl. Mech. 82 (11), 111005. http://dx.doi.org/10.1115/1.4031049.

Anindita, S.N., Conti, R., Zauchner, D., Paunović, N., Qiu, W., Buzhor, M.G., Krivitsky, A., Luo, Z., Müller, R., Grützmacher, H., et al., 2023. Tough PEG-only hydrogels with complex 3D structure enabled by digital light processing of "all-PEG" resins. Aggregate 4 (6), e368. http://dx.doi.org/10.1002/agt2.368.

Barenblatt, G.I., 1959. The formation of equilibrium cracks during brittle fracture. General ideas and hypotheses. Axially-symmetric cracks. J. Appl. Math. Mech. 23 (3), 622–636. http://dx.doi.org/10.1016/0021-8928(59)90157-1.

Barenblatt, G.I., 1962. The mathematical theory of equilibrium cracks in brittle fracture. Adv. Appl. Mech. 7, 55–129. http://dx.doi.org/10.1016/S0065-2156(08)70121-2.

Bazant, Z.P., Le, J.-L., Salviato, M., 2021. Quasibrittle Fracture Mechanics and Size Effect: A First Course. Oxford University Press.

Bertrand, T., Peixinho, J., Mukhopadhyay, S., MacMinn, C.W., 2016. Dynamics of swelling and drying in a spherical gel. Phys. Rev. Appl. 6 (6), 064010. http://dx.doi.org/10.1103/PhysRevApplied.6.064010.

Bhattacharya, S., Shunmugam, R., 2020. Unraveling the effect of PEG chain length on the physical properties and toxicant removal capacities of cross-linked network synthesized by Thiol–Norbornene photoclick chemistry. ACS Omega 5 (6), 2800–2810. http://dx.doi.org/10.1021/acsomega.9b03554.

Bird, R.B., Stewart, W.E., Lightfoot, E.N., 2006. Transport Phenomena. Wiley.

Böger, L., Keip, M.-A., Miehe, C., 2017. Minimization and saddle-point principles for the phase-field modeling of fracture in hydrogels. Comput. Mater. Sci. 138, 474–485. http://dx.doi.org/10.1016/j.commatsci.2017.06.010.

Bouklas, N., Huang, R., 2012. Swelling kinetics of polymer gels: comparison of linear and nonlinear theories. Soft Matter 8 (31), 8194–8203. http://dx.doi.org/10.1039/C2SM25467K.

Bourdin, B., Francfort, G.A., Marigo, J.-J., 2000. Numerical experiments in revisited brittle fracture. J. Mech. Phys. Solids 48 (4), 797–826. http://dx.doi.org/10.1016/S0022-5096(99)00028-9.

Chen, S., Huang, R., Ravi-Chandar, K., 2020. Linear and nonlinear poroelastic analysis of swelling and drying behavior of gelatin-based hydrogels. Int. J. Solids Struct. 195, 43–56. http://dx.doi.org/10.1016/j.ijsolstr.2020.03.017.

Chester, S.A., Anand, L., 2010. A coupled theory of fluid permeation and large deformations for elastomeric materials. J. Mech. Phys. Solids 58 (11), 1879–1906. http://dx.doi.org/10.1016/j.jmps.2010.07.020.

Choo, J., Sun, W., 2018. Cracking and damage from crystallization in pores: Coupled chemo-hydro-mechanics and phase-field modeling. Comput. Methods Appl. Mech. Engrg. 335, 347–379. http://dx.doi.org/10.1016/j.cma.2018.01.044.

Choo, J., Sun, Y., Fei, F., 2023. Size effects on the strength and cracking behavior of flawed rocks under uniaxial compression: From laboratory scale to field scale. Acta Geotech. 18 (7), 3451–3468. http://dx.doi.org/10.1007/s11440-023-01806-7.

Chung, J.Y., Regev, I., Mahadevan, L., 2016. Spontaneous exfoliation of a drying gel. Soft Matter 12 (37), 7855–7862. http://dx.doi.org/10.1039/C6SM01011C.

Ding, J., Remmers, J.J., Leszczynski, S., Huyghe, J.M., 2018. Swelling driven crack propagation in large deformation in ionized hydrogel. J. Appl. Mech. 85 (2), 021007. http://dx.doi.org/10.1115/1.4038698.

Dortdivanlioglu, B., Linder, C., 2019. Diffusion-driven swelling-induced instabilities of hydrogels. J. Mech. Phys. Solids 125, 38–52. http://dx.doi.org/10.1016/j.jmps.2018.12.010.

Flory, P.J., 1942. Thermodynamics of high polymer solutions. J. Chem. Phys. 10 (1), 51–61. http://dx.doi.org/10.1063/1.1723621.

Flory, P.J., Rehner, J., 1943. Statistical mechanics of cross-linked polymer networks II. Swelling. J. Chem. Phys. 11 (11), 521–526. http://dx.doi.org/10.1063/1.1723792.

Francfort, G., Marigo, J.-J., 1998. Revisiting brittle fracture as an energy minimization problem. J. Mech. Phys. Solids 46 (8), 1319–1342. http://dx.doi.org/10.1016/S0022-5096(98)00034-9.

Hong, W., Zhao, X., Zhou, J., Suo, Z., 2008. A theory of coupled diffusion and large deformation in polymeric gels. J. Mech. Phys. Solids 56 (5), 1779–1793. http://dx.doi.org/10.1016/j.jmps.2007.11.010.

Huggins, M.L., 1941. Solutions of long chain compounds. J. Chem. Phys. 9 (5), 440–440. http://dx.doi.org/10.1063/1.1750930.

Kuhn, C., Müller, R., 2008. A phase field model for fracture. Proceedings in Applied Mathematics and Mechanics 8, 10223–10224. http://dx.doi.org/10.1002/pamm.200810223.

Kuhn, C., Müller, R., 2010. A continuum phase field model for fracture. Eng. Fract. Mech. 77 (18), 3625–3634. http://dx.doi.org/10.1016/j.engfracmech.2010.08.009.

Leslie, K.-A., Doane-Solomon, R., Arora, S., Curley, S.J., Szczepanski, C., Driscoll, M.M., 2021. Gel rupture during dynamic swelling. Soft Matter 17 (6), 1513–1520. http://dx.doi.org/10.1039/D0SM01718C.

Levin, M., Tang, Y., Eisenbach, C.D., Valentine, M.T., Cohen, N., 2024. Understanding the response of poly(ethylene glycol) diacrylate (PEGDA) hydrogel networks: A statistical mechanics-based framework. Macromolecules 57 (15), 7074–7086. http://dx.doi.org/10.1021/acs.macromol.3c02635.

Luo, C., Sanavia, L., De Lorenzis, L., 2023. Phase-field modeling of drying-induced cracks: Choice of coupling and study of homogeneous and localized damage. Comput. Methods Appl. Mech. Engrg. 410, 115962. http://dx.doi.org/10.1016/j.cma.2023.115962.

Mao, Y., Anand, L., 2018. A theory for fracture of polymeric gels. J. Mech. Phys. Solids 115, 30–53. http://dx.doi.org/10.1016/j.jmps.2018.02.008.

Miehe, C., Hofacker, M., Welschinger, F., 2010a. A phase field model for rate-independent crack propagation: Robust algorithmic implementation based on operator splits. Comput. Methods Appl. Mech. Engrg. 199 (45–48), 2765–2778. http://dx.doi.org/10.1016/j.cma.2010.04.011.

Miehe, C., Mauthe, S., Teichtmeister, S., 2015a. Minimization principles for the coupled problem of Darcy–Biot-type fluid transport in porous media linked to phase field modeling of fracture. J. Mech. Phys. Solids 82, 186–217. http://dx.doi.org/10.1016/j.jmps.2015.04.006.

Miehe, C., Mauthe, S., Ulmer, H., 2014. Formulation and numerical exploitation of mixed variational principles for coupled problems of Cahn–Hilliard-type and standard diffusion in elastic solids. Internat. J. Numer. Methods Engrg. 99 (10), 737–762. http://dx.doi.org/10.1002/nme.4700.

Miehe, C., Schaenzel, L.-M., Ulmer, H., 2015b. Phase field modeling of fracture in multi-physics problems. Part I. Balance of crack surface and failure criteria for brittle crack propagation in thermo-elastic solids. Comput. Methods Appl. Mech. Engrg. 294, 449–485. http://dx.doi.org/10.1016/j.cma.2014.11.016.

Miehe, C., Welschinger, F., Hofacker, M., 2010b. Thermodynamically consistent phase-field models of fracture: Variational principles and multi-field FE implementations. Internat. J. Numer. Methods Engrg. 83 (10), 1273–1311. http://dx.doi.org/10.1002/nme.2861.

Moës, N., Dolbow, J., Belytschko, T., 1999. A finite element method for crack growth without remeshing. Internat. J. Numer. Methods Engrg. 46 (1), 131–150. http://dx.doi.org/10.1002/(SICI)1097-0207(19990910)46:1<131::AID-NME726>3.0.CO;2-J.

Mora, T., Boudaoud, A., 2006. Buckling of swelling gels. Eur. Phys. J. E 20, 119–124. http://dx.doi.org/10.1140/epje/i2005-10124-5.

Noselli, G., Lucantonio, A., McMeeking, R.M., DeSimone, A., 2016. Poroelastic toughening in polymer gels: A theoretical and numerical study. J. Mech. Phys. Solids 94, 33–46. http://dx.doi.org/10.1016/j.jmps.2016.04.017.

Plummer, A., Adkins, C., Louf, J.-F., Košmrlj, A., Datta, S.S., 2024. Obstructed swelling and fracture of hydrogels. Soft Matter 20 (7), 1425–1437. http://dx.doi.org/10.1039/D3SM01470C.

Pruksawan, S., Lim, J.W.R., Lee, Y.L., Lin, Z., Chee, H.L., Chong, Y.T., Chi, H., Wang, F., 2023. Enhancing hydrogel toughness by uniform cross-linking using modified polyhedral oligomeric silsesquioxane. Commun. Mater. 4 (1), 75. http://dx.doi.org/10.1038/s43246-023-00402-2.

Qiu, Y., Park, K., 2001. Environment-sensitive hydrogels for drug delivery. Adv. Drug Deliv. Rev. 53 (3), 321–339. http://dx.doi.org/10.1016/S0169-409X(01)00203-4.

de Silva, U.K., Lapitsky, Y., 2016. Preparation and timed release properties of self-rupturing gels. ACS Appl. Mater. Interfaces 8 (42), 29015–29024. http://dx.doi.org/10.1021/acsami.6b09370.

Steck, J., Hassan, S., Suo, Z., 2023. Fracture initiated from corners in brittle soft materials. J. Mech. Phys. Solids 170, 105115. http://dx.doi.org/10.1016/j.jmps.2022.105115.

Tada, H., Paris, P.C., Irwin, G.R., 1973. The stress analysis of cracks handbook. Del Research Corporation.

Tanaka, T., Fillmore, D.J., 1979. Kinetics of swelling of gels. J. Chem. Phys. 70 (3), 1214–1218. http://dx.doi.org/10.1063/1.437602.

VanZanten, A., Chen, S.-Y., Driscoll, M.M., Szczepanski, C.R., 2024. Unconstrained dynamic gel swelling generates transient surface deformations. Soft Matter 20 (34), 6742–6753. http://dx.doi.org/10.1039/D4SM00762J.

Wang, Z., Ye, Q., Yu, S., Akhavan, B., 2023. Poly ethylene glycol (PEG)-based hydrogels for drug delivery in cancer therapy: a comprehensive review. Adv. Heal. Mater. 12 (18), 2300105. http://dx.doi.org/10.1002/adhm.202300105.

Weiss, F., Cai, S., Hu, Y., Kyoo Kang, M., Huang, R., Suo, Z., 2013. Creases and wrinkles on the surface of a swollen gel. J. Appl. Phys. 114, 073507. http://dx.doi.org/10.1063/1.4818943.

Wilson, Z.A., Borden, M.J., Landis, C.M., 2013. A phase-field model for fracture in piezoelectric ceramics. Int. J. Fract. 183 (2), 135–153. http://dx.doi.org/10.1007/s10704-013-9881-9.

Xue, T., Adriaenssens, S., Mao, S., 2021. Mapped phase field method for brittle fracture. Comput. Methods Appl. Mech. Engrg. 385, 114046. http://dx.doi.org/10.1016/j.cma.2021.114046.

Xue, T., Liao, S., Gan, Z., Park, C., Xie, X., Liu, W.K., Cao, J., 2023. JAX-FEM: A differentiable GPU-accelerated 3D finite element solver for automatic inverse design and mechanistic data science. Comput. Phys. Comm. 291, 108802. http://dx.doi.org/10.1016/j.cpc.2023.108802.

Yoon, J., Cai, S., Suo, Z., Hayward, R.C., 2010. Poroelastic swelling kinetics of thin hydrogel layers: comparison of theory and experiment. Soft Matter 6 (23), 6004–6012. http://dx.doi.org/10.1039/C0SM00434K.

Yu, Y., Landis, C.M., Huang, R., 2018. Steady-state crack growth in polymer gels: a linear poroelastic analysis. J. Mech. Phys. Solids 118, 15–39. http://dx.doi.org/10.1016/j.jmps.2018.05.008.

Yuan, W., Zhao, Y., Zhang, B., 2025. A poromechanical framework for hydraulic fracturing processes in transversely isotropic rocks. Acta Geotech. 20, 2049–2073. http://dx.doi.org/10.1007/s11440-025-02541-x.

Zhang, X., Zhong, Z., 2017. A coupled theory for chemically active and deformable solids with mass diffusion and heat conduction. J. Mech. Phys. Solids 107, 49–75. http://dx.doi.org/10.1016/j.jmps.2017.06.013.

Zheng, S., Huang, R., Lin, R., Liu, Z., 2022. A phase field solution for modelling hyperelastic material and hydrogel fracture in ABAQUS. Eng. Fract. Mech. 276, 108894. http://dx.doi.org/10.1016/j.engfracmech.2022.108894.